Computer-Aided Civil and Infrastructure Engineering **23** (2008) 339–359

Damage Identification of a Composite Beam Using Finite Element Model Updating

B. Moaveni, X. He & J. P. Conte*

Department of Structural Engineering, University of California at San Diego, USA

&

Raymond A. de Callafon

Department of Mechanical and Aerospace Engineering, University of California at San Diego, USA

Abstract: *The damage identification study presented in this article leveraged a full-scale sub-component experiment conducted in the Charles Lee Powell Structural Research Laboratories at the University of California, San Diego. As a payload project attached to a quasi-static test of a full-scale composite beam, a high-quality set of low-amplitude vibration response data was acquired from the beam at various damage levels. The Eigensystem Realization Algorithm was applied to identify the modal parameters (natural frequencies, damping ratios, displacement and macro-strain mode shapes) of the composite beam based on its impulse responses recorded in its undamaged and various damaged states using accelerometers and long-gage fiber Bragg grating strain sensors. These identified modal parameters are then used to identify the damage in the beam through a finite element model updating procedure. The identified damage is consistent with the observed damage in the composite beam.*

1 INTRODUCTION

In recent years, structural health monitoring has received increased attention in the civil engineering research community with the objective to identify structural damage at the earliest possible stage and evaluate the remaining useful life (damage prognosis) of structures. Vibration-based, non-destructive damage identification is based on changes in the dynamic characteristics (e.g., modal parameters) of a structure as a basis for identifying structural damage. Experimental modal analysis (EMA) has been used as a technology for identifying the modal parameters of a structure based on its measured vibration data. It should be emphasized that the success of damage identification based on EMA depends strongly on the accuracy and completeness of the identified structural dynamic properties. Extensive literature reviews on vibration-based damage identification were provided by Doebling et al. (1996, 1998) and Sohn et al. (2003).

Damage identification consists of detecting the occurrence of damage, localizing the damage zones, and estimating the extent of damage. Numerous vibration-based methods have been proposed to achieve these goals. Salawu (1997) presented a review on the use of changes in natural frequencies for damage detection only. However, it is in general impossible to localize damage (i.e., obtain spatial information on the structural damage) from changes in natural frequencies only. Pandey et al. (1991) introduced the concept of using curvature mode shapes for damage localization. In their study, by using a cantilever and a simply supported analytical beam model, they demonstrated the effectiveness of employing changes in curvature mode shapes

*To whom correspondence should be addressed. E-mail: *jpconte@ucsd.edu.*

as a damage indicator for detecting and localizing damage. Bernal and Gunes (2004) have incorporated changes in modal flexibility matrices (or flexibility proportional matrices) into the damage locating vector (DLV) technique to localize damage. Recently, Adeli and Jiang (2006) presented a novel multi-paradigm dynamic time-delay fuzzy wavelet neural network (WNN) model for non-parametric identification of structures using the nonlinear auto-regressive moving average with exogenous inputs (NARMAX) approach. Jiang and Adeli (2005, 2007) applied this WNN model to high-rise building structures, for both nonlinear systems and damage identification. Methods based on changes in identified modal parameters to detect and localize damage have also been further developed for the purpose of damage quantification. Among these methods are strain-energy based methods (Shi et al., 2002) and the direct stiffness calculation method (Maeck and De Roeck, 1999). Another class of sophisticated methods consists of applying sensitivity-based finite element (FE) model updating for damage identification (Friswell and Mottershead, 1995). These methods update the physical parameter of a FE model of the structure by minimizing an objective function expressing the discrepancy between analytically predicted and experimentally identified features that are sensitive to damage such as natural frequencies and mode shapes. Optimum solutions of the problem are reached through sensitivity-based optimization algorithms. In recent years, sensitivity-based FE model updating techniques have been applied successfully for condition assessment of structures (Teughels and De Roeck, 2004).

The study presented in this article, which is an extension of an already published conference paper (Moaveni et al., 2006), leveraged a full-scale sub-component experiment conducted in the Charles Lee Powell Structural Research Laboratories at the University of California, San Diego (UCSD). As a payload project attached to a quasi-static test of a full-scale composite beam, the authors acquired a high-quality set of low-amplitude vibration response data from the beam at various damage levels. The Eigensystem Realization Algorithm (ERA) (Juang and Pappa, 1985) was applied to identify the modal parameters (natural frequencies, damping ratios, displacement and macro-strain mode shapes) of the composite beam based on its impulse responses recorded in its undamaged and various damaged states using accelerometers and long-gage fiber Bragg grating strain sensors. These identified modal parameters are presented and compared at different levels of damage. They are then used to identify damage in the beam using a sensitivity-based finite element model updating procedure.

2 COMPOSITE BEAM EXPERIMENT

The designed I-5/Gilman Advanced Technology Bridge is a 137 m (450 ft) long cable-stayed bridge supported by a 59 m (193 ft) high A-frame pylon, and utilizing fiber reinforced polymer (FRP) composite materials. The bridge system is a dual plane, asymmetric cable-stayed design as shown in Figure 1. Before the I-5/Gilman Advanced Technology Bridge can be constructed, a Validation Test Program to evaluate the performance of the bridge was performed. The prototype test program, which was conducted at the Charles Lee Powell Structural Research Laboratories at UCSD, evaluated the manufactured

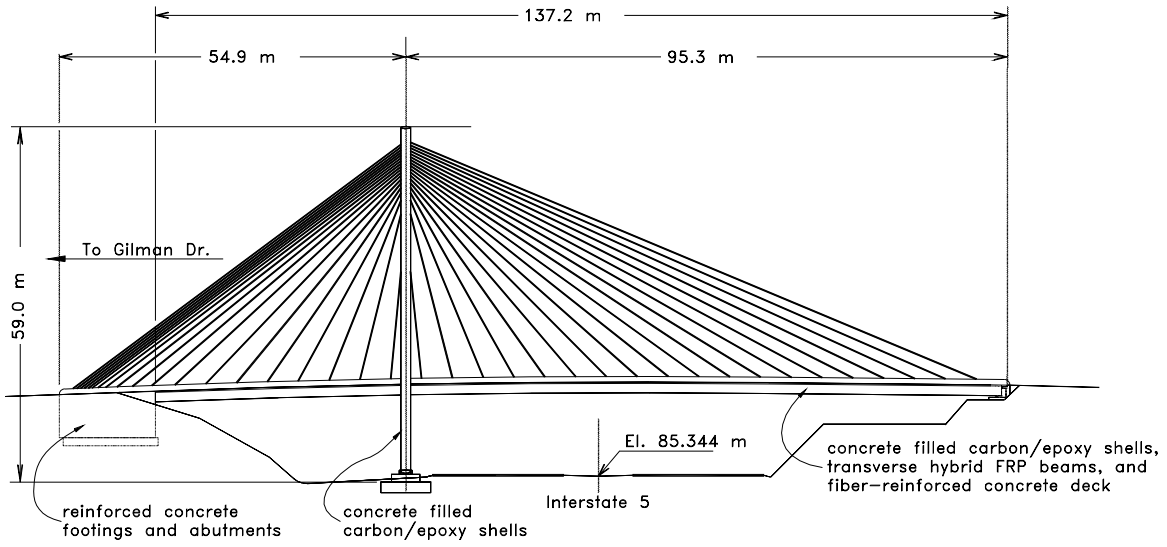

Fig. 1. Elevation of I-5/Gilman Advanced Technology Bridge (Brestel et al., 2003).

FRP components at the material level, through coupon testing and other non-destructive techniques on the members, and at the element level on full-scale sub-component, connection and system tests (Brestel et al., 2003). The test leveraged in this study was conducted on a full-scale sub-component longitudinal girder of the bridge (Test L2). The objective of this experiment was to validate the design of a concrete-filled composite beam component of the planned I-5/Gilman Advanced Technology Bridge (Seible et al., 1996). For this purpose, uni-directional quasi-static cyclic load tests (i.e., load-unload cycles) of increasing amplitude were applied to the beam, gradually introducing damage. After each of several sequences of loading-unloading cycles, a set of low-amplitude dynamic tests was performed to investigate the changes in dynamic characteristics (extracted from the vibration response data) as a function of increasing structural damage. For this purpose, two different sources of dynamic excitation were used, namely (1) a computer-controlled electro-dynamic shaker, and (2) an impact hammer. The vibration data obtained from the impact tests were revealed to be the most informative to identify the beam modal parameters at different levels of damage. The small-strain vibration response data was measured at several damage levels using a set of four long-gage (1 m) fiber Bragg grating (FBG) strain sensors and a set of eight single channel piezoelectric accelerometers.

2.1 Test setup

The longitudinal girders for the I-5/Gilman Advanced Technology Bridge consist of prefabricated carbon/epoxy shells filled with concrete. In the second phase of the longitudinal girder test program, which is considered in this study, a girder shell specimen (L2) of diameter 0.91 m (3 ft) and length 9.75 m (32 ft) was cut into two equal halves, spliced together at mid-span with mild steel reinforcement, and filled with concrete (see Figures 2 and 3). The splice using longitudinal steel reinforcement

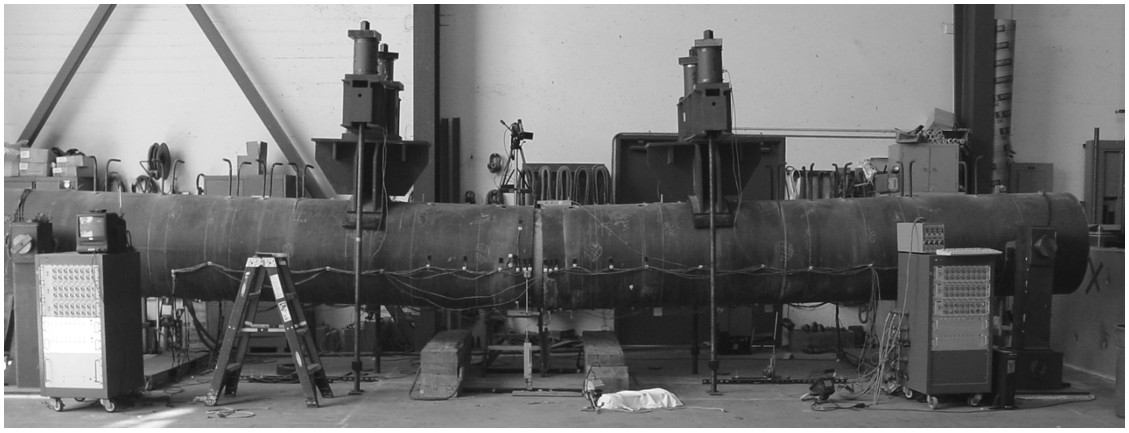

Fig. 2. Elevation view of the tested composite beam.

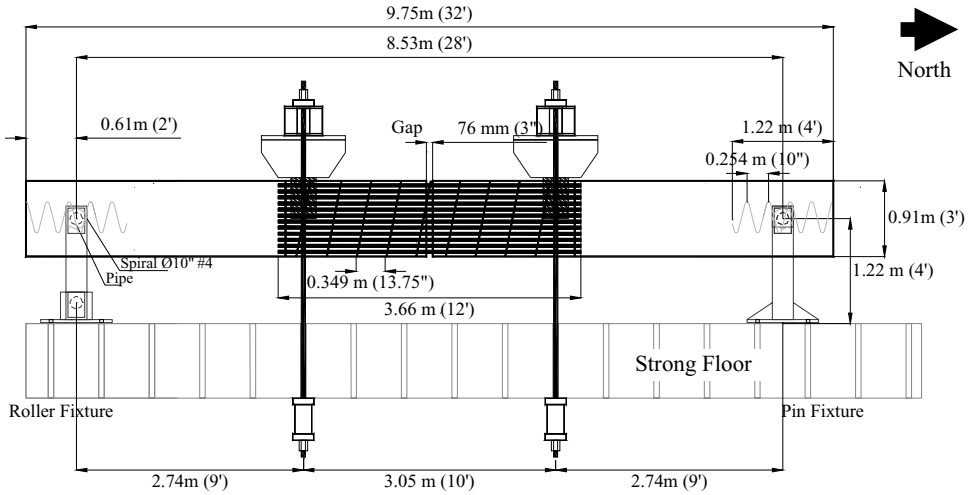

Fig. 3. Schematic test setup: Side elevation (Brestel et al., 2003).

Table 1
Loading protocol

Loading cycle number	*Load cycle target*	*Peak total load (kN)*
1	1,000 kN	1,016
2	1,000 kN*	
3	F'_y	1,779
4	$\mu_\Delta = 1.0$	2,278
5	$\mu_\Delta = 1.0$*	
6	3,000 $\mu\varepsilon$ tensile strain	2,713
7	$\mu_\Delta = 1.5$	2,761
	$\mu_\Delta = 1.5$*	
8	$\mu_\Delta = 2.0$	3,066
	$\mu_\Delta = 2.0$*	
9	$\mu_\Delta = 3.0$	3,516
10	$\mu_\Delta = 3.0$	
11	$\mu_\Delta = 3.0$	
	$\mu_\Delta = 4.0$	3,743
12	$\mu_\Delta = 4.0$*	

*At the end of these cycles, the load fixtures were removed and a set of dynamic tests were performed.

allows a ductile behavior of the connection. In the FRP shell, two rows of 51 mm (2 in) diameter holes were drilled along the top edge of the girder and shear stirrups were embedded in the concrete core to provide interfacial shear resistance between the girder and the deck.

A uni-directional quasi-static cyclic loading was applied to the girder using four 1,335 kN (300 kips) displacement-controlled hydraulic actuators in a four-point bending test (see Figure 3). Initially, the girder was loaded to a total of 1,000 kN (225 kips) to establish a well-lubricated pin connection at the supports of the simply supported girder. The increasing level of the cyclic load progressively introduced damage in the beam through inelastic (irreversible) deformations. The loading history for the test is summarized in Table 1 and the plot of the total load applied versus the girder vertical displacement at mid-span is shown in Figure 4. The load cycle targets for the initial yield (F'_y) and the displacement ductility levels ($\mu_\Delta = 1.0$, 1.5, 2.0, 3.0, and 4.0) were determined pre-test from moment-curvature analyses. More details of the test setup are provided by Brestel et al. (2003). After load cycles 2, 5, 7, 8, and 12, the loading fixtures were removed to perform a sequence of dynamic tests for system and damage identification studies. This sequence of dynamic tests was performed twice before starting the quasi-static loading cycles and the corresponding undamaged states of the beam are referred to as states S0 and S1. States S2–S6 refer to the state of the beam after loading cycles 2, 5, 7, 8, and 12, respectively, shown in Figure 4. The repeated sequence of dynamic tests consisted of a set of forced vibration tests using a 0.22 kN (50 lbs) force electro-dynamic shaker followed by a set of impact (free vibration) tests using an impact hammer with integrated load cell recording the applied force. The forced vibration tests performed using the shaker consist of a set of sixteen (Gaussian) white noise excitations followed by three (linear) sine sweeps across the frequency ranges 12–22 Hz, 38–48 Hz, and 93–103 Hz, respectively. These three frequency ranges were selected so as to excite the first three vibration modes of the beam, the frequencies of which were predicted using a finite element

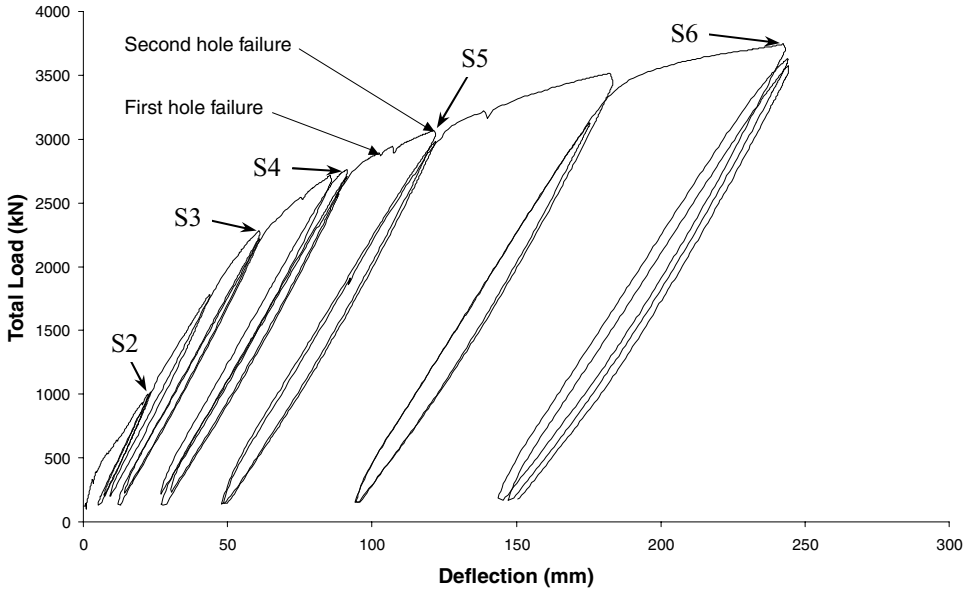

Fig. 4. Total load versus girder vertical displacement at mid-span.

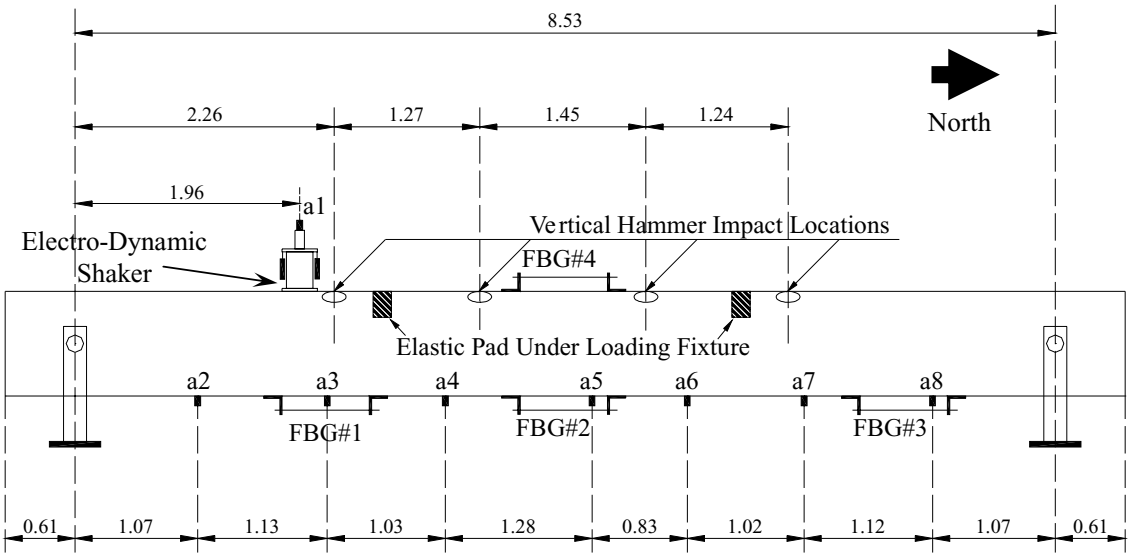

Fig. 5. Locations of accelerometers, FBG sensors, vertical hammer impacts, and electro-dynamic shaker.

model of the beam. The free vibration tests conducted using the impact hammer consisted of three vertical impact tests at each of four locations along the top edge of the girder as shown in Figure 5. Therefore, a total of 12 vertical impact tests were performed on the beam for each of seven different states (S0–S6). It was found that the shaker-induced vibration data were of considerably lower amplitude than the impact response data, resulting in a much lower signal-to-noise ratio. Therefore, the modal identification results presented in this article are based only on the data collected from the vertical impact tests.

2.2 Instrumentation

The girder was instrumented with strain gages, linear potentiometers, and inclinometers for the entire duration of the quasi-static cyclic tests. In addition, the girder was instrumented with four long-gage fiber Bragg grating (FBG) strain sensors (1 m gage length) and eight accelerometers with the required sensitivity/accuracy for the purpose of the (low-amplitude) payload dynamic tests. The FBG strain sensors were surface mounted using brackets, with a pair of sensors located along the top and bottom of the beam at mid-span, and the remaining two sensors located along the bottom edge of the beam at approximately 1/3 of the beam length on either side of mid-span as shown in Figure 5. The FBG strain sensors were pre-strained in their long-gage packages to measure compression as well as tension. In addition to the FBG strain sensors, eight accelerometers were attached to the girder specimen to measure vertical acceleration. Seven of these accelerometers were approximately equally spaced along the bottom edge of the girder and one was mounted on the moving mass of the electro-dynamic shaker to measure the dynamic force applied to the beam (see Figure 5). The technical characteristics of the accelerometers are: PCB model 393A03, amplitude range: 5 g pk, frequency range (10%) 0.3-4,000 Hz, resolution 5×10^{-6} g pk, voltage sensitivity 1,000 mV/g, excitation voltage 18–30 VDC. For every dynamic test performed at each of the states S0–S6, the vibration response of the composite girder was measured by accelerometers a2–a8, whereas the four FBG strain sensors measured the vibration response for states S1–S5 only. Figure 6 illustrates the acceleration (left-hand column) and FBG strain (right-hand column) measurements after an impact applied at location 1 (see Figure 5) at state S1. Figure 7 shows the Fourier Amplitude Spectra (FSA) of two acceleration and two FBG strain measurements for the same impact test.

3 IDENTIFICATION OF MODAL PARAMETERS

In this study, the Eigensystem Realization Algorithm (ERA) (Juang and Pappa, 1985) followed by a least squares optimization (De Callafon et al., 2008) was employed for identifying the modal parameters (natural frequencies, damping ratios, displacement, and macro-strain mode shapes) of the composite beam in its undamaged and damaged states. The identified modal parameters using ERA are based on the impact test (free vibration) data recorded by the accelerometers or FBG strain sensors, separately. Because two separate data acquisition systems, not time-synchronized and with

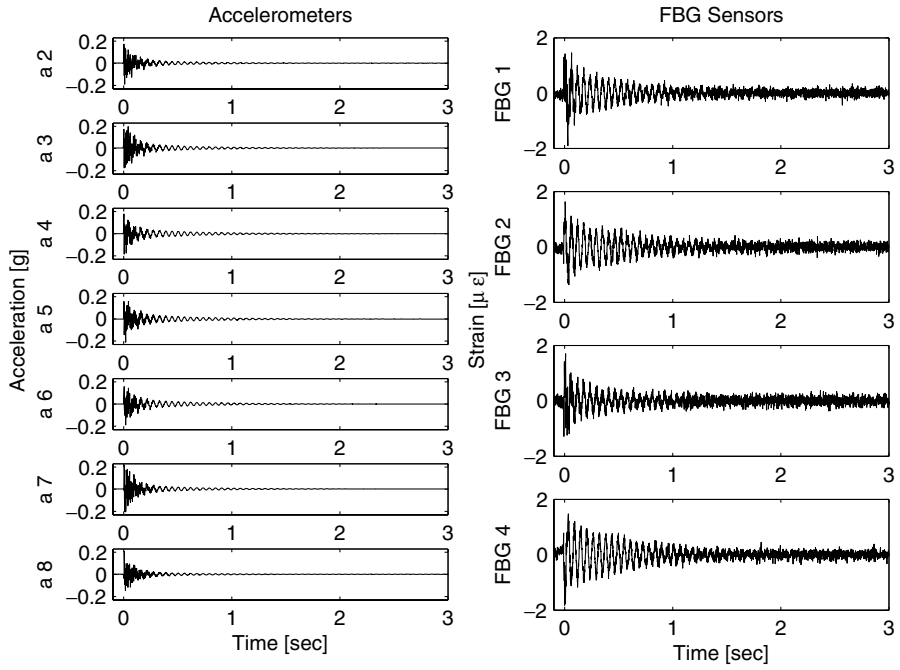

Fig. 6. Acceleration and FBG strain measurements during Test 1 at state S1.

different sampling rates, were used to collect the acceleration and macro-strain data, it was more convenient to apply ERA to the two types of measurements separately. A total of 12 vertical impact tests were performed on the beam at each of the seven states S0–S6, with states S0 and S1 representing the beam in its undamaged condition. Two different cases of modal identification are performed at each damage state, namely, (1) ERA is applied to a single test data (i.e., one test at a time), and (2) ERA is applied to all 12 impact test data in a single identification.

3.1 Identified modal parameters based on accelerometer data

Figure 8 shows the natural frequencies of the first five modes identified using ERA based on accelerometer data for each of $12 \times 7 = 84$ impact tests (each circle corresponds to an identified frequency from one impact test). In each ERA realization (considering one test at a time), a Hankel matrix of size $(7 \times 250) \times 250$ was constructed based on the impulse response data sampled at 512 Hz. Then, after performing a singular value

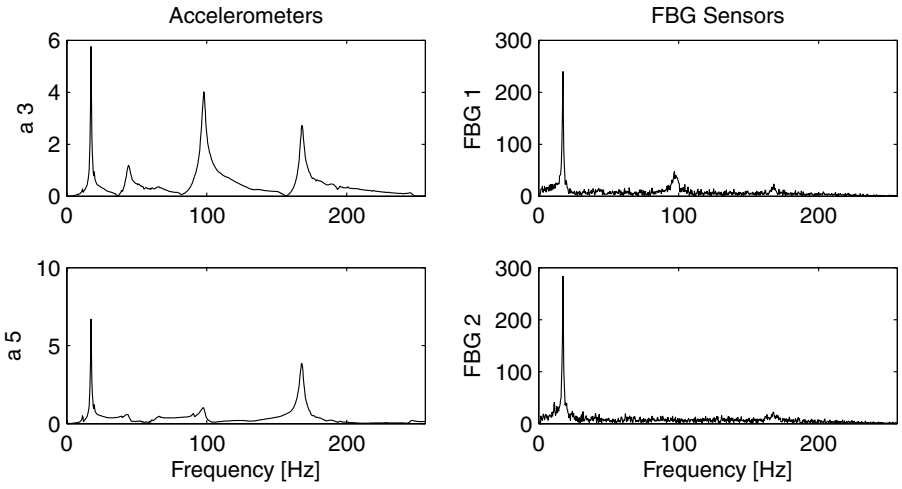

Fig. 7. Fourier amplitude spectra of some acceleration and FBG strain measurements during Test 1 at state S1.

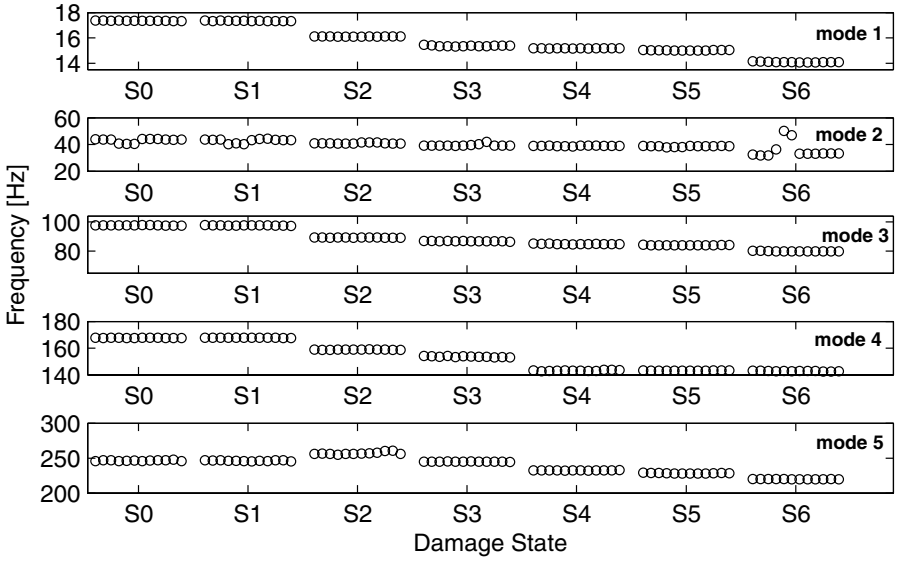

Fig. 8. Identified natural frequencies of the first five vibration modes using ERA based on acceleration data (12 separate identifications at each damage state).

decomposition, a system of order $n = 16$ was realized based on the natural frequency stabilization diagram (Peeters and De Roeck, 2001), from which a maximum of eight physical modes of vibration could be extracted. From Figure 8, it is observed that: (1) At each damage state, the modal frequencies identified from each of the 12 impact tests are generally in close agreement. The few cases when an identified modal frequency is not consistent with the others could be explained by a low participation of the corresponding vibration mode (e.g., impact applied near a modal node) resulting in a low signal-to-noise ratio. (2) As expected, the identified natural frequencies for states S0 and S1 are almost identical, because both sets of results correspond to the undamaged state of the beam. (3) With increasing level of damage in the beam, the identified modal frequencies decrease (with an exception for the fifth mode at state S2), consistent with the stiffness degradation due to damage. It should be noted that the changes in the natural frequencies due to structural damage are much more significant than the variability (due to changes in location and amplitude of the impact force as well as the estimation uncertainty) of the identified natural frequencies within one damage state. The statistics (mean and coefficient-of-variation) of the identified modal frequencies (based on 12 identifications) are reported in Table 2, whereas Table 3 provides the same statistics for the identified damping ratios. The coefficient-of-variation of a random variable is defined as the ratio of its standard deviation to its (absolute) mean value.

The second case of system identification was performed based on the same acceleration data, but including the data from all 12 impact tests (at each damage state) in a single identification. The basic idea behind this identification strategy is to use simultaneously the information from all impact tests to identify the modal parameters. Therefore, if a single test does not contain significant information about a vibration mode (for example, due to its low modal participation), this mode can still be identified well through other impact test data

Table 2
Mean (Hz)/coefficient-of-variation (%) of the natural frequencies identified using ERA based on acceleration data for states S0–S6

	S0	*S1*	*S2*	*S3*	*S4*	*S5*	*S6*
Mode 1	17.35/0.1	17.34/0.1	16.10/0.1	15.37/0.2	15.17/0.1	15.02/0.1	14.09/0.2
Mode 2	42.97/3.5	42.78/3.5	40.93/0.8	39.47/2.2	38.93/0.5	38.58/0.9	35.68/17.2
Mode 3	97.58/0.1	97.49/0.1	89.26/0.1	86.82/0.2	84.90/0.2	84.05/0.2	79.91/0.2
Mode 4	167.67/0.0	167.72/0.0	158.87/0.1	153.64/0.3	143.23/0.2	143.21/0.1	142.81/0.1
Mode 5	246.42/0.3	246.22/0.3	255.91/0.1	244.85/0.1	232.39/0.1	228.35/0.2	219.80/0.1

Table 3
Mean (%)/coefficient-of-variation (%) of the damping ratios identified using ERA based on acceleration data for states S0–S6 (sets of 12 impact tests)

	S0	*S1*	*S2*	*S3*	*S4*	*S5*	*S6*
Mode 1	1.5/2.7	1.5/3.3	1.6/3.4	1.7/7.3	1.2/3.7	1.3/2.6	1.4/2.4
Mode 2	4.0/47.3	4.1/53.7	2.9/27.9	2.9/89.6	2.2/8.8	2.8/6.8	5.5/77.0
Mode 3	1.7/7.0	1.7/6.1	2.0/6.1	1.7/2.0	2.1/17.1	2.1/28.5	1.7/2.1
Mode 4	0.9/4.0	0.8/2.3	0.9/2.1	1.7/19.3	1.8/9.9	0.9/3.0	1.5/7.9
Mode 5	0.8/82.7	0.7/36.6	0.6/39.3	0.7/16.6	0.8/10.5	0.9/9.1	0.9/11.2

that are more informative about this mode. For this purpose, ERA is applied in its multiple input, multiple output (MIMO) formulation (Juang and Pappa, 1985), but instead of forming the Hankel matrix based on free vibration data from a truly multiple input test, the block Hankel matrix is formed by including the response measurements from (r) single input impact tests as

$$\mathbf{H} = \begin{bmatrix} \begin{bmatrix} \mathbf{g}^1(1) & \mathbf{g}^2(1) & \cdots & \mathbf{g}^r(1) \\ \mathbf{g}^1(2) & \mathbf{g}^2(2) & \cdots & \mathbf{g}^r(2) \\ \cdots & \cdots & \cdots & \cdots \\ \mathbf{g}^1(N) & \mathbf{g}^2(N) & \cdots & \mathbf{g}^r(N) \end{bmatrix} \begin{bmatrix} \mathbf{g}^1(2) & \cdots & \mathbf{g}^r(2) \\ \mathbf{g}^1(3) & \cdots & \mathbf{g}^r(3) \\ \cdots & \cdots & \cdots \\ \mathbf{g}^1(N+1) & \cdots & \mathbf{g}^r(N+1) \end{bmatrix} \cdots \begin{bmatrix} \mathbf{g}^1(N) & \cdots & \mathbf{g}^r(N) \\ \mathbf{g}^1(N+1) & \cdots & \mathbf{g}^r(N+1) \\ \cdots & \cdots & \cdots \\ \mathbf{g}^1(2N-1) & \cdots & \mathbf{g}^r(2N-1) \end{bmatrix} \\ \cdots \end{bmatrix}, \quad (1)$$

where $\mathbf{g}^i(k)$ denotes the impulse response vector (at time $t = k\Delta T$) from the ith impact test. In this case, the block Hankel matrix was built including the data from all 12 impact tests ($r = 12$) at each damage state. A model of order $n = 16$ (from which a maximum of eight physical vibration modes could be extracted) was realized from the data, and then the modal parameters were extracted from this state-space model. The natural frequencies and damping ratios identified using this approach are reported in Table 4 for all damage states considered. Figure 9 shows the normalized mode shapes (projection of complex mode shapes on the real axis) corresponding to state S1 (undamaged state of the beam). In Figure 9, the circles correspond to the identified mode shape at the sensor locations and the dashed lines represent cubic spline interpolation through the circles. It should be noted that, due to flexibility of the support structures relative to the beam, the mode shapes of the beam-support system are generally not zero at the support locations. The equivalent stiffness of the two support structures was calculated based on their geometric and material properties and was included in the FE model of the beam-support system.

Figure 10 plots the identified complex-valued mode shapes in polar plots (i.e., complex plane). This representation indicates the degree of non-proportional damping of a vibration mode. If the components (each representing an observed degree of freedom) of a complex-valued mode shape are collinear (i.e., in phase or out of phase), then this mode is classically (or proportionally) damped. Scattering of the components of a mode shape in the

Table 4
Natural frequencies (Hz) and damping ratios (%) identified using ERA based on acceleration data at states S0–S6 (all 12 impact tests considered in a single identification)

	Mode 1		*Mode 2*		*Mode 3*		*Mode 4*		*Mode 5*	
	Frequency (Hz)	*Damping ratio (%)*	*Frequency (Hz)*	*Damping ratio (%)*	*Frequency (Hz)*	*Damping ratio (%)*	*Frequency (Hz)*	*Damping ratio (%)*	*Frequency (Hz)*	*Damping ratio (%)*
S0	17.35	1.5	43.48	4.3	97.57	1.7	167.70	0.8	246.63	0.4
S1	17.34	1.5	43.24	4.6	97.50	1.7	167.74	0.8	246.16	0.5
S2	16.09	1.7	40.72	2.7	89.24	2.0	158.90	0.9	254.51	1.1
S3	15.35	1.7	39.09	2.0	86.80	1.7	153.32	1.8	244.72	0.6
S4	15.17	1.3	38.91	2.2	84.82	2.2	143.24	1.3	232.25	0.8
S5	15.00	1.3	38.98	3.2	84.12	1.9	143.20	0.9	227.94	0.9

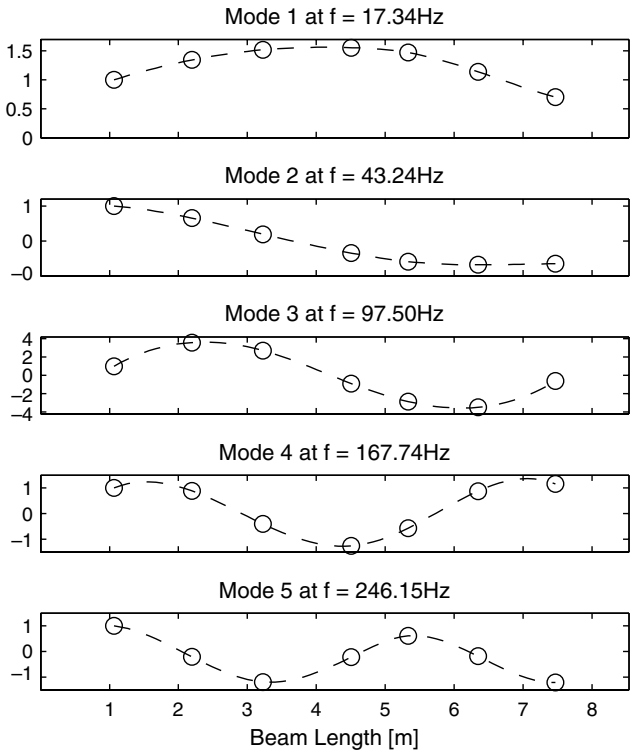

Fig. 9. Normalized (real) mode shapes of the composite beam at state S1.

complex plane indicates that the mode is non-classically damped. From Figure 10, it is observed that the first four identified modes are classically damped and the fifth identified mode is non-classically damped. It should be noted that due to low signal-to-noise ratio and/or identification or modeling errors, a truly classically damped mode could be identified as non-classically damped. Figure 11 provides a comparison of the impulse response (impact applied at location 1) simulated using the realized model with the corresponding response measured by accelerometers a2, a4, and a6 (see Figure 5) at state S1, and the modal decomposition of the simulated acceleration impulse response. This modal decomposition is obtained from the realized model of the system (De Callafon et al., 2007). This figure shows that: (1) the simulated and measured impulse responses are in excellent agreement, indicating the accuracy of the realized model, and (2) the fifth vibration mode does not contribute significantly to the total response of the system and is therefore characterized by a lower signal-to-noise ratio than the other modes. This could explain the non-classical damping characteristics identified for the fifth mode (see Figure 10). The first four mode shapes identified (from a single state-space model realized based on all twelve impact test data) at three increasing levels of damage (S0, S2, and S4) are shown in Figure 12. It is observed that the damage-induced changes in these mode shapes are small. However, as shown in the damage identification section, these small changes in some of the mode shapes are sufficient to identify (localize) damage based on finite element model updating.

3.2 Identified modal parameters based on FBG strain sensor data

The impulse response data transduced from the FBG strain sensors were also used to identify the modal parameters of the composite beam in the two identification cases defined in Section 3. Figure 13 shows the natural frequencies identified using ERA based on impact test data measured from the four FBG sensors at states S1–S5. It should be recalled that the FBG strain sensors were not available during the dynamic tests performed at the first and last damage states of the beam (S0 and S6). From Figure 13, it is observed that some of the vibration modes cannot be identified from some impact tests. For example, at state S4, the second and fourth modal frequencies could not be identified and also the third mode was only identified for the first three and last three of the 12 impact tests (impacts at locations one and four in Figure 5). Table 5 provides the statistics (mean and coefficient-of-variation) of the identified modal frequencies based on sets of 12 impact tests (considered one at a time) at beam states S1–S5. By comparing the identified modal frequencies obtained from accelerometer data with those obtained from FBG strain sensor data, it is observed that the second natural frequency is identified with less variability from acceleration data than from macro-strain data, and the fifth natural frequency can only be identified from the acceleration data. Table 6

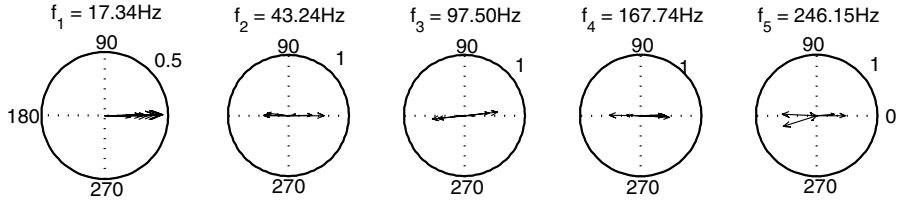

Fig. 10. Complex-valued (displacement) mode shapes in polar plots at state S1.

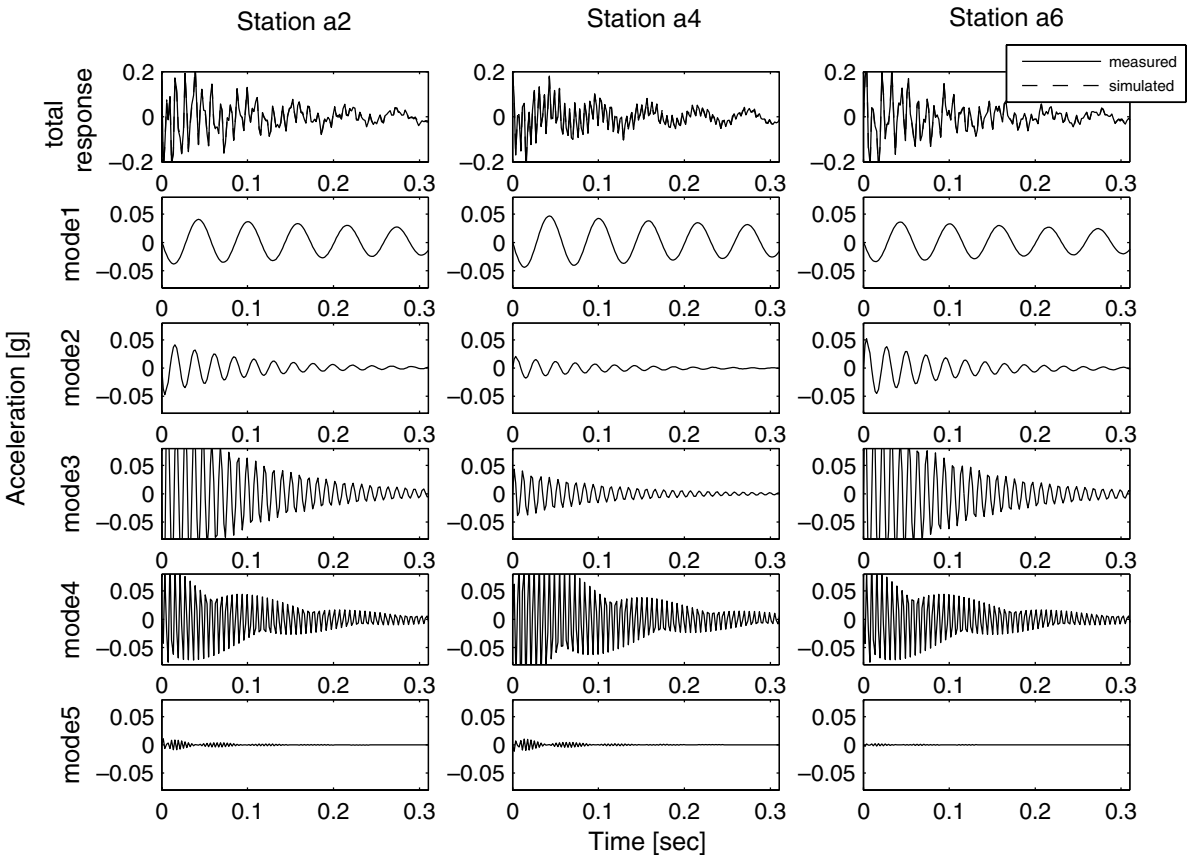

Fig. 11. Modal decomposition of impulse response measured by accelerometers a2, a4, and a6 at state S1.

reports the natural frequencies and damping ratios identified at states S1–S5 based on all 12 impact test FBG sensor data considered at once. It is observed that these identified natural frequencies and damping ratios are in good agreement with their counterparts obtained from acceleration data (see Table 4), except for the second mode. The corresponding identified macro-strain mode shapes are represented in polar plots in Figure 14 for state S1. The fact that vibration modes 2, 3, and 4 are identified as non-classically damped could be due to the low contribution of these modes to the total response. Figure 15 shows the identified macro-strain mode shapes projected on the real axis and normalized to a unit length for states S1, S2, S3, and S5. The second and fourth macro-strain modes could not be identified at state S3. From Figure 15, it is observed that the macro-strain mode shapes at FBG sensor #2 (see Figure 5) change significantly due to damage beyond state S2. Figure 16 shows a comparison of the impulse response (impact applied at location 1) simulated using the realized model with the corresponding response measured by the four FBG strain sensors at state S1, and the modal decomposition of the simulated beam macro-strain impulse response. This figure indicates clearly that: (1) the simulated and measured impulse responses are in very good agreement, validating the accuracy of the realized model, and (2) the contributions of modes 2, 3, and 4 to the total impulse response are much smaller than that of the first mode.

4 SENSITIVITY OF IDENTIFIED MODAL PARAMETERS TO DAMAGE

This section investigates the changes in identified natural frequencies and modal assurance criterion (MAC) values (between corresponding mode shapes in undamaged and damaged states) with an increasing level of damage in the beam. MAC values are bounded between 0 and 1 and measure the degree of correlation between corresponding mode shapes in the undamaged and damaged states (MAC value of 1 for unchanged mode shapes). Based on the force-displacement curve for the quasi-static tests shown in Figure 4, the global tangent stiffness K of the beam structure is determined at several points corresponding to states S0–S6 along the envelope curve of the hysteresis loops. The normalized changes in tangent stiffness ΔK_{Si} and normalized changes in modal frequencies $\Delta f^{k}_{\mathrm{Si}}$ are defined, respectively as

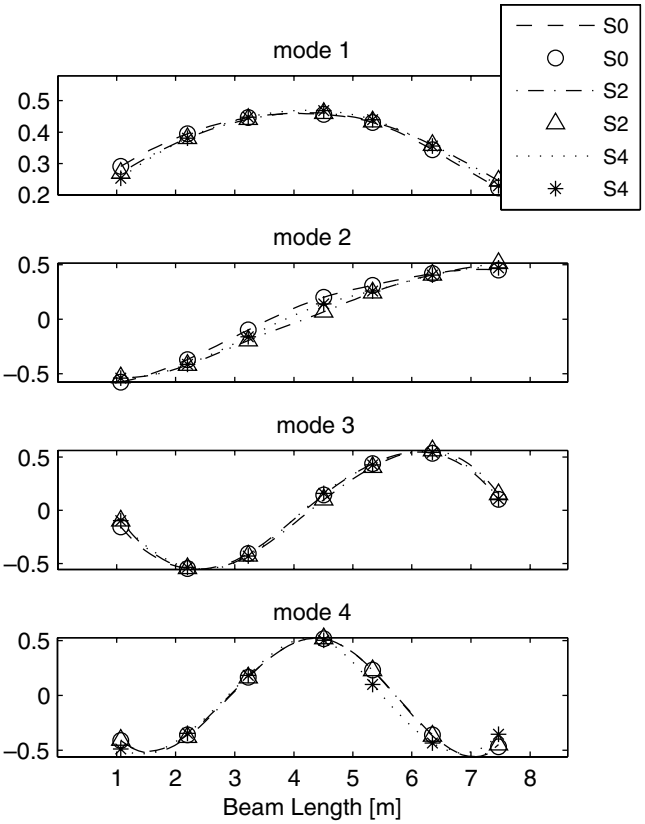

Fig. 12. Normalized (real) mode shapes of the composite beam at states S0, S2, and S4.

$$\Delta K_{\mathrm{Si}} = \frac{K_{\mathrm{S0}} - K_{\mathrm{Si}}}{K_{\mathrm{S0}}}, \quad \Delta f_{\mathrm{Si}}^{k} = \frac{f_{\mathrm{S0}}^{k} - f_{\mathrm{Si}}^{k}}{f_{\mathrm{S0}}^{k}} \qquad (2)$$

in which the subscript Si denotes the damage state of the beam (e.g., S0, S1, . . . , S6), K_{Si} represents the tangent stiffness at state Si, and f_{Si}^{k} denotes the identified natural frequency of the kth vibration mode at state Si. The normalized changes in tangent stiffness and natural frequencies are plotted in Figure 17 versus the damage level (S0–S6). It is observed that with increasing level of damage, the tangent stiffness and natural frequencies of the first five identified modes decrease monotonically, with an exception for the fifth mode at state S2. MAC values are calculated between the identified mode shapes at each state of the beam (S0–S6) and the corresponding mode shapes at the undamaged state (S0) of the beam. Figure 18 displays the calculated MAC values for the first four vibration modes identified at states S0–S6 (top plot) and the relative changes of these MAC values, $\Delta\mathrm{MAC} = 1 - \mathrm{MAC}_{\mathrm{Si}}^{k}$, as a function of damage level (bottom plot). From this figure, it is observed that: (1) the MAC value of the first mode has the least sensitivity to damage, whereas the MAC value of the second mode is the most sensitive to damage, which is consistent with the observed changes in normalized displacement mode shapes shown in Figure 12. (2) The MAC values obtained at states S4 and S6 are outliers of the trend between MAC value and damage level. From the changes in modal frequencies and MAC values, it is possible to detect the presence of damage, but it is very difficult (if not impossible) to determine the location and extent of damage, because both of these indicators are global in nature (i.e., aggregated quantities).

Table 5
Mean (Hz)/coefficient-of-variation (%) of the natural frequencies identified using ERA based on FBG sensor macro-strain data at states S1– S5 (sets of 12 impact tests)

	S1	*S2*	*S3*	*S4*	*S5*
Mode 1	17.35/0.1	16.13/0.1	15.46/0.3	15.25/0.7	15.04/0.1
Mode 2	40.77/4.2	39.46/4.7	36.94/5.5	NA	36.76/6.4
Mode 3	96.98/0.5	88.89/0.4	86.86/0.4	84.39/1.4	81.12/3.4
Mode 4	167.56/0.1	158.77/0.1	152.35/0.3	NA	143.19/0.1

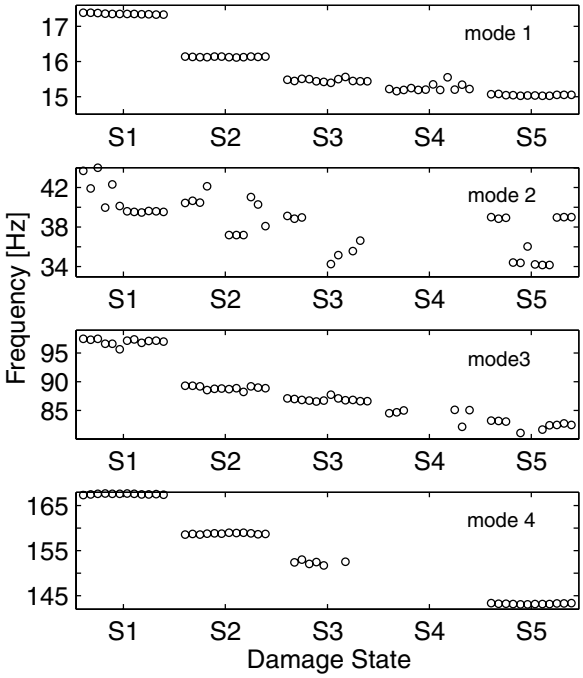

Fig. 13. Identified natural frequencies of the first four modes using ERA based on FBG sensor data at states S1–S5 (12 identifications at each damage state).

5 DAMAGE IDENTIFICATION BASED ON FINITE ELEMENT MODEL UPDATING

Based on the identified modal parameters of the composite beam, an element-by-element sensitivity-based finite

Table 6
Natural frequencies (Hz) and damping ratios (%) identified using ERA based on FBG sensor macro-strain data at states S1–S5 (all 12 impact tests considered in a single identification)

	Mode 1		*Mode 2*		*Mode 3*		*Mode 4*	
	Frequency (Hz)	*Damping ratio (%)*	*Frequency (Hz)*	*Damping ratio (%)*	*Frequency (Hz)*	*Damping ratio (%)*	*Frequency (Hz)*	*Damping ratio (%)*
S1	17.35	1.5	39.52	1.1	97.29	1.6	167.66	0.8
S2	16.12	1.6	37.13	0.6	89.06	2.0	158.86	0.9
S3	15.45	1.6	NA	NA	86.76	1.7	NA	NA
S4	15.17	1.0	NA	NA	NA	NA	NA	NA
S5	15.07	1.1	34.23	0.7	81.07	1.5	143.10	1.0

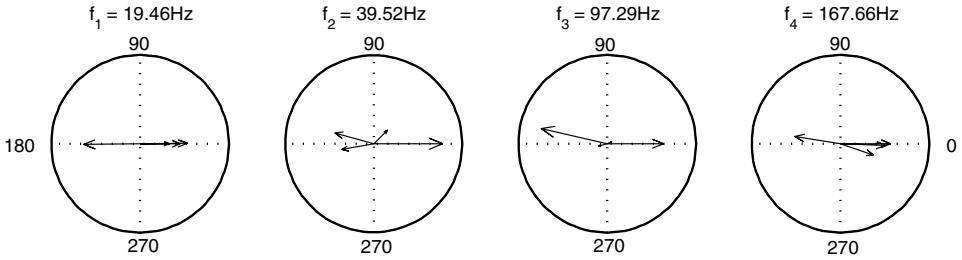

Fig. 14. Complex-valued macro-strain mode shapes in polar plots at state S1.

element (FE) model updating approach (Conte and Liu, 2001; Teughels and De Roeck, 2004) was used to identify (detect, localize, and quantify) the damage in the beam at various damage levels. Two separate cases of damage identification were performed using FE model updating: (1) the residuals used in the updating process are based on the natural frequencies and displacement mode shapes identified from the accelerometer data, and (2) the residuals used in the updating process are based on the natural frequencies, displacement mode shapes identified from the accelerometer data, and macro-strain mode shapes identified from the FBG strain sensor data. In both cases, damage in the beam at the various damage levels is identified as a change in stiffness (modulus of elasticity) in the finite elements. For this purpose, a linear elastic FE model of the composite beam was developed in FEDEASLab (Filippou and Constantinides, 2004) using 10 Bernoulli-Euler beam elements for the composite beam (elements 1–10) and two truss elements to model the flexible end supports (elements 11 and 12) as shown in Figure 19. Both truss elements are pinned at their base (nodes 12 and 13) and the top node (node 2) of the left support (element 11) is restrained in the horizontal direction (along the beam). Nodes 3 to 9 are at the location of accelerometers a2–a8 along the beam (see Figure 19). The beam elements (1–10) are assumed to have a constant mass density of 2,320 Kg/m^3, whereas no mass is assigned to the truss elements (11–12). The element section properties are reported in Table 7, where A and I denote the assigned cross-section area and moment of inertia, respectively. These two section properties are equivalent section properties accounting for the concrete (confined), composite, and steel (longitudinal reinforcement)

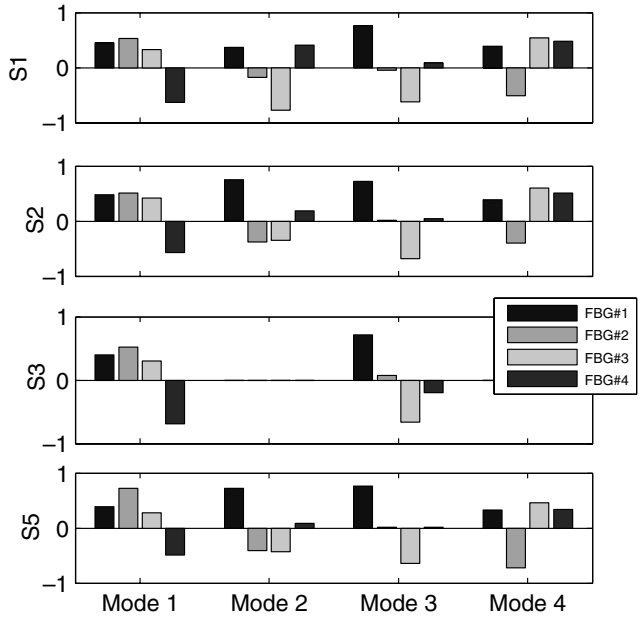

Fig. 15. Normalized macro-strain mode shapes for states S1, S2, S3, and S5.

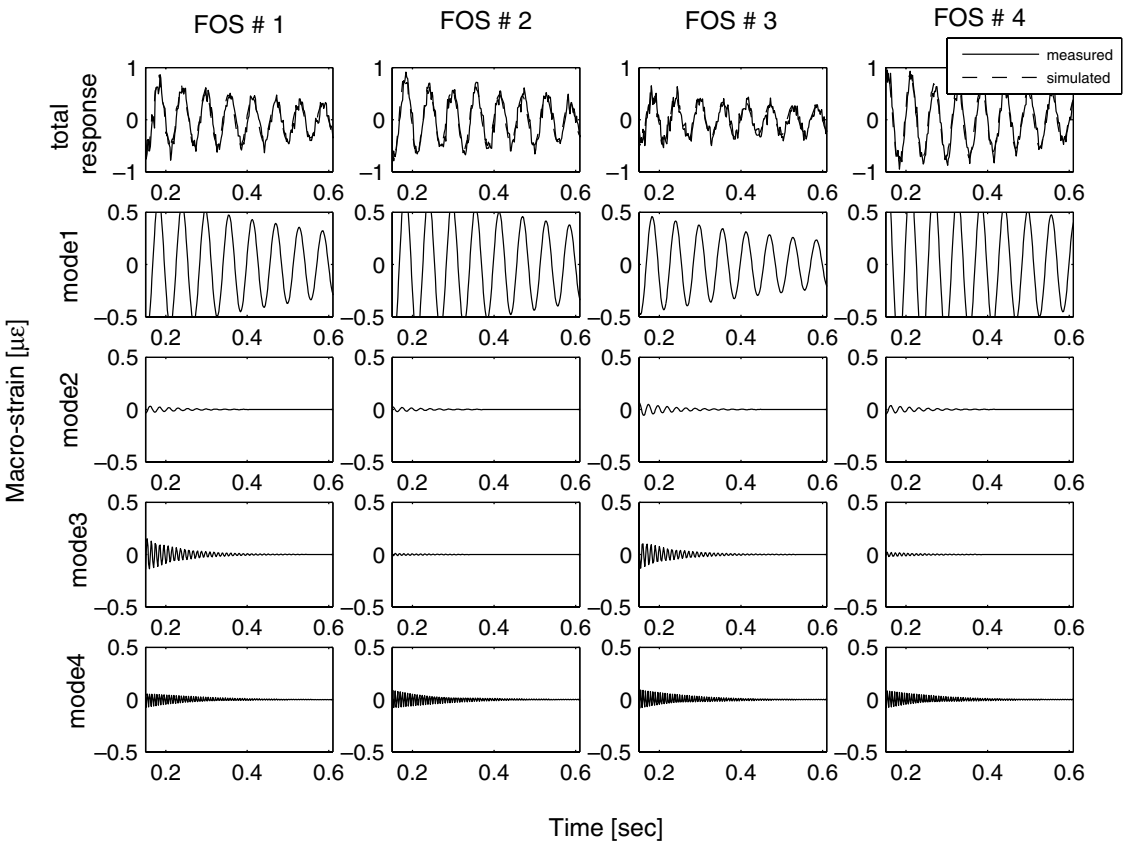

Fig. 16. Modal decomposition of impulse response measured by FBG strain sensors 1–4 at state S1.

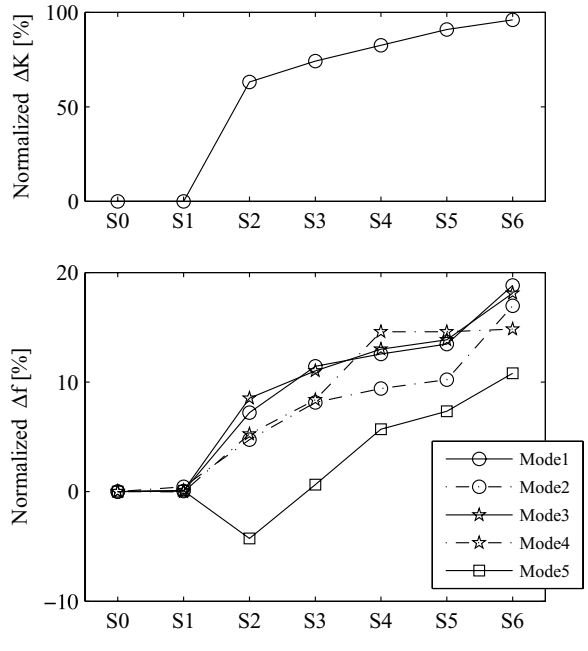

Fig. 17. Normalized changes in tangent stiffness (top plot) and natural frequencies (bottom plot) versus damage level.

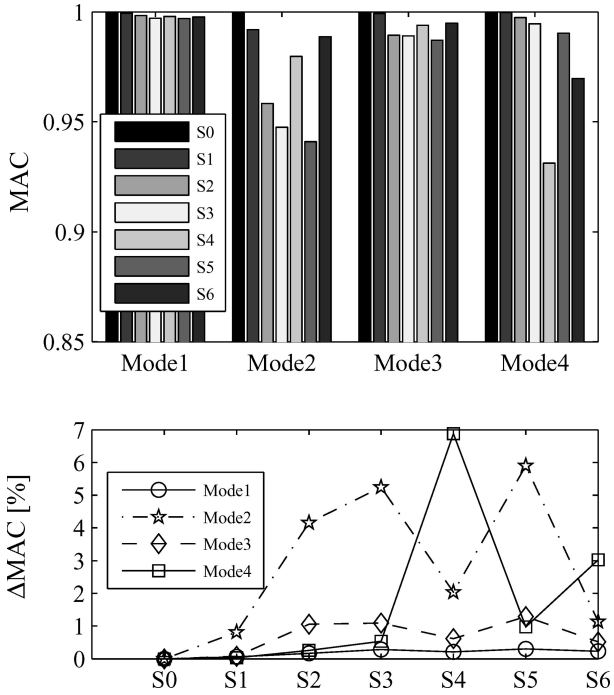

Fig. 18. MAC values (top plot) and their relative changes (bottom plot) at different damage levels.

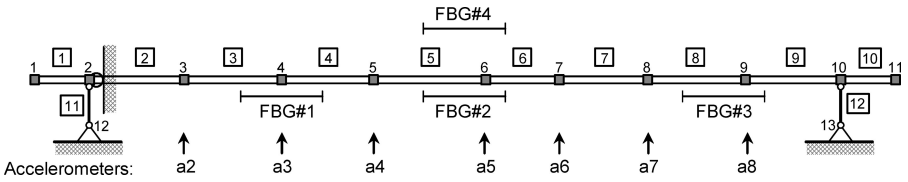

Fig. 19. Finite element model of the beam in FEDEASLab showing element and node numbers, locations of accelerometers, and FBG strain sensors.

materials. Elements 4–7 have a larger cross-section area to account for the longitudinal steel reinforcement at half-span (see Figure 3). The first step to identify damage in the beam is to obtain a reference (baseline) FE model based on the modal parameters identified at the undamaged state of the beam (state S1). In this study, the reference model was obtained through updating the moduli of elasticity of all 12 elements from their nominal values using residuals based on the natural frequencies and displacement mode shapes of the first five modes identified from accelerometer data. The updated values for the moduli of elasticity in the reference model (E^{ref}) for all 12 elements are also reported in Table 7. It should be noted that the updating parameters (moduli of elasticity) act as effective moduli of elasticity reflecting the overall stiffness of the structure, including the contributions of the structural components that are not directly (or accurately) represented in the FE model or the parameters of which are not updated. The low (unrealistic) values of the effective moduli of elasticity found for elements 1 and 10 are due to: (1) the fact that the confinement of the composite shell is much less effective at the ends of the beam than along the beam, and (2) the fact that the selected residuals are not sensitive to the updating parameters of elements 1 and 10. The lack of symmetry in the calibrated effective moduli of elasticity of the beam elements can be due to variability in the quality of concrete and concrete filling within the composite shell. After a reference/baseline model is obtained, the effective moduli of elasticity of elements 3, 4, 5, 6, 7, 8, 11, and 12 (total of eight elements) are updated at states S2–S6 through minimization of an objective function. It should be noted that elements 1 and 10 are located outside of the two supports and therefore did not experience any damage during the quasi-static loading of the beam. In addition, the modal parameters used in the updating process (natural frequencies, displacement and macro-strain mode shapes) are lowly sensitive to changes in the moduli of elasticity of elements 2 and 9. Also, because there were no sensors between nodes 3 and 12 (foot of left support) as well as between nodes 9 and 13 (foot of right support), the use of the moduli of elasticity of all four elements 2, 9, 11, and 12 as updating parameters would result in compensation effects between elements 2 and 11 as well as between elements 9 and 12. Therefore, the moduli of elasticity of elements 1, 2, 9, and 10 were not used as updating parameters. However, the installation of more sensors along the beam, especially at the location of the supports, would have resulted in more refined damage identification results (in terms of the spatial distribution of damage). After completion of all the tests, the carbon shell was cut and removed to assess the quality of the infilled concrete and the extent of damage. No significant damage was observed at the location of elements 2 and 9.

The objective (cost) function used in this study for damage identification based on FE model updating is given by

$$f = \frac{1}{2}\mathbf{r}^T\mathbf{W}\mathbf{r} \tag{3}$$

where $\mathbf{r}$ denotes the residual vector, expressing the discrepancy between experimentally identified modal parameters and their analytically predicted (using the FE model) counterparts, and $\mathbf{W}$ is a diagonal weighting matrix with each diagonal component inversely proportional to the standard deviation of the natural frequency of the corresponding vibration mode based on the 12 identifications at each damage state (see Table 2). The residual vector can be partitioned as $\mathbf{r} = \left[\begin{smallmatrix}\mathbf{r}_f \\ \mathbf{r}_s\end{smallmatrix}\right]$ where $\mathbf{r}_f$

Table 7
Element section properties for all 12 elements (El.)

	El. 1	*El. 2*	*El. 3*	*El. 4*	*El. 5*	*El. 6*	*El. 7*	*El. 8*	*El. 9*	*El. 10*	*El. 11*	*El. 12*
E^{ref}(GPa)	2.76	51.71	59.15	38.41	42.06	32.31	50.91	38.68	51.71	2.76	57.18	132.92
A (m^2)	0.732	0.732	0.732	0.872	0.872	0.872	0.872	0.732	0.732	0.732	0.0026	0.0026
I (m^4)	0.0298	0.0298	0.0298	0.0436	0.0436	0.0436	0.0436	0.0298	0.0298	0.0298	0	0

and $\mathbf{r}_s$ define eigenfrequency and mode shape residuals, respectively, as

$$\mathbf{r}_f = \left[\frac{\lambda_j - \tilde{\lambda}_j}{\tilde{\lambda}_j}\right], \qquad \mathbf{r}_s = \left[\frac{\phi_j^l}{\phi_j^r} - \frac{\tilde{\phi}_j^l}{\tilde{\phi}_j^r}\right] \quad j = 1, \ldots, n_m, \tag{4}$$

where λ_j and $\tilde{\lambda}_j$ denote the analytical and experimental eigenvalues corresponding to the jth vibration mode, respectively, with $\lambda_j = \omega_j^2$ and ω_j = natural frequency; ϕ_j and $\tilde{\phi}_j$ denote the analytical and experimentally identified mode shape vectors, respectively. In Equation (4), the superscript r indicates a reference component of a mode shape vector (with respect to which the other components of the mode shape are normalized), the superscript l refers to the components that are used in the updating process (i.e., at the locations of the accelerometers or FBG strain sensors), and n_m denotes the number of vibration modes considered in the residual vector.

In the first case of damage identification, the natural frequencies and displacement mode shapes of the first five modes (see Figure 9) identified from acceleration data are used to form the residual vector which has a total of 35 residual components consisting of 5 eigenfrequency and $5 \times (7-1) = 30$ displacement mode shape residuals. The model parameters (effective moduli of elasticity) of the reference model are updated from state S1 (reference model) through S6. In the second case of damage identification, in addition to the natural frequencies and displacement mode shapes of the first five vibration modes identified based on acceleration data, the macro-strain mode shapes of the first four vibration modes identified based on FBG strain sensor data are considered in the residual vector for a total of 47 residual components consisting of 5 eigenfrequency, 30 displacement mode shape, and $4 \times (4-1) = 12$ macro-strain mode shape residuals. The reference model (which is the same for both damage identification cases) is updated at states S2, S3, and S5. It should be mentioned that the macro-strains obtained from the FBG sensors at state S4 were significantly noisier than at the other states (due to the fact that the FBG sensors were not re-tensioned at this damage state) and therefore the FE model was not updated at this damage state. In the second case of damage identification, the mode shape residual vector consists of two parts: residuals from displacement mode shapes ($\mathbf{r}_s^{acc}$) and residuals from macro-strain mode shapes ($\mathbf{r}_s^{ms}$), as $\mathbf{r}_s = \left[\begin{smallmatrix}\mathbf{r}_s^{acc} \\ \mathbf{r}_s^{ms}\end{smallmatrix}\right]$, where both parts are defined separately as in the second part of Equation (4). The analytical macro-strain mode shapes are derived from the displacement mode shapes through a transformation matrix $\mathbf{T}^{ms}$. This matrix connects the nodal degrees of freedom (DOFs) of the FE model to the deformation of the FBG sensors based on linear elastic Bernoulli–Euler beam theory with exact displacement interpolation functions (Conte and Liu, 2001).

The (dimensionless) damage factor of element e is defined as

$$a^{\mathrm{e}} = \frac{E^{\mathrm{e}}_{\mathrm{undamaged}} - E^{\mathrm{e}}_{\mathrm{damaged}}}{E^{\mathrm{e}}_{\mathrm{undamaged}}}, \tag{5}$$

where E^{e} is the effective modulus of elasticity of element e. At each damage state, the damage factors for elements 3, 4, 5, 6, 7, 8, 11, and 12 are updated to minimize the objective function f defined in Equation (3) based on a trust region Gauss–Newton optimization algorithm (Coleman and Li, 1996). The damage factors were constrained to be in the range $[-\infty\ 1]$ for calibrating the reference model at state S1 to result in positive moduli of elasticity. For updating the FE model at states S2–S6, the relative damage factor defined as $a^{\mathrm{e}}_{\mathrm{rel}} = (E^{\mathrm{e}}_{\mathrm{previous\_state}} - E^{\mathrm{e}}_{\mathrm{current\_state}})/E^{\mathrm{e}}_{\mathrm{previous\_state}}$ was constrained to be in the range $[-0.2\ \ 0.9]$. The upper-bound of 90% was selected based on the observed damage in the beam (i.e., it remained far from $a^{\mathrm{e}}_{\mathrm{rel}} = 0.9$ even at the end of the quasi-static tests), whereas the lower bound of –20% was selected considering that the identified effective moduli of elasticity are not expected to increase beyond 20% between two consecutive damage states. The optimization process was performed using the function "fmincon" in Matlab (Mathworks, 2005), with Jacobian and first-order estimate of the Hessian matrices calculated analytically based on the sensitivities of modal parameters to the updating variables (Fox and Kapoor, 1968). It should be noted that the Fox and Kapoor's sensitivity formulas apply only for translational DOFs in the mode shapes. The sensitivities of rotational DOFs, which are required in the second case of damage identification for macro-strain mode shapes, were calculated based on the work of Conte and Liu (2001).

Table 8 reports the values of the updated effective moduli of elasticity (E^e) for elements 3–8, 11, 12 (see Figure 19) as well as the damage factors of these elements calculated relative to the reference/baseline state S1 at states S2–S6 for the first case of damage identification. For each state S2–S6, Table 9 presents the experimentally identified modal frequencies together with their analytical counterparts obtained from the updated FE model as well as the MAC values between experimental and analytical mode shapes for the first case of damage identification. It should be noted that the analytical mode shapes were truncated at the locations of the accelerometers to match the size of the experimental mode shapes. From Table 9, it is observed that: (1) the experimentally identified modal parameters match very well their analytical counterparts, especially for the first four vibration

Table 8
Effective moduli of elasticity E^e(GPa)/damage factors a^e(%) (relative to reference state S1) of updated elements (# 3–8, 11, 12) at states S2–S6 for first case of damage identification

	El. 3	*El. 4*	*El. 5*	*El. 6*	*El. 7*	*El. 8*	*El. 11*	*El. 12*
S2	46.30/21.7	31.35/18.4	34.30/18.5	31.41/2.8	49.60/2.6	32.15/16.9	61.82/–8.1	72.78/45.2
S3	39.44/33.3	35.92/6.5	27.30/35.1	30.68/5.1	48.36/5.0	30.19/21.9	58.16/1.7	59.84/55.0
S4	27.52/53.5	35.42/7.8	24.36/42.1	33.49/–3.6	52.48/–3.1	28.01/27.6	55.52/2.9	70.82/46.7
S5	27.64/53.3	39.27/–2.2	24.30/42.2	26.93/16.6	43.56/14.4	27.62/28.6	58.80/–2.8	74.91/43.6
S6	33.17/43.9	26.72/30.4	24.50/41.8	25.81/20.1	32.55/36.1	25.39/34.4	36.28/36.5	77.91/41.4

modes, (2) the discrepancies between analytical (from updated FE model) and experimental modal parameters tend to increase with increasing damage, and (3) at each damage state, the largest discrepancies between analytical and experimental modal parameters are exhibited by the fifth vibration mode. This is due to the fact that: (1) this mode has the lowest modal contribution to the total measured acceleration response (see Figure 10), (2) the estimation variability of the identified modal parameters is relatively large for this mode compared to the other modes (see Section 3), and therefore smaller weights are assigned to the fifth mode residuals in the objective function. It should be noted that the modal parameters of the fifth vibration mode were not used in the FE model updating process at state S2. Figure 20 shows a bar plot of the updated values of E^e for beam elements 1–10 (as explained above) at states S1 to S6 for the first case of damage identification. It is recalled that the effective moduli of elasticity of elements 1, 2, 9, 10 are not updated beyond state S1. From the results presented in Table 8 and Figure 20, it is observed that the effective moduli of elasticity display an overall decreasing trend with increasing level of damage. There are some exceptions to this decreasing trend in some beam elements, which can be due to: (1) measurement errors and estimation variability of the identified modal parameters, (2) low sensitivity of the residuals to some of the updating parameters (E^e), (3) modeling errors and uncertainties, and (4) optimization errors in the FE model updating process (i.e., local but not global minimum).

For the second case of damage identification, Table 10 gives the updated E^e for the updating elements (# 3–8, 11, 12) and the corresponding damage factors (relative to the reference state S1) at states S2, S3, and S5, whereas Figure 21 shows in a bar plot the updated E^e for all beam elements at states S1, S2, S3, and S5. Table 11

Table 9
Comparison of experimental and analytical modal frequencies (Hz) and MAC values between experimental and analytical mode shapes at states S1–S6 (first case of damage identification)

		Mode 1	*Mode 2*	*Mode 3*	*Mode 4*	*Mode 5*
S1	Freq. (experiment)	17.34	43.24	97.50	167.74	246.15
	Freq. (updated model)	17.31	43.28	97.80	167.74	245.02
	MAC	0.999	0.998	0.997	0.993	0.839
S2	Freq. (experiment)	16.09	40.72	89.24	158.90	–
	Freq. (updated model)	16.08	40.97	89.16	158.93	–
	MAC	1.000	0.999	0.994	0.993	–
S3	Freq. (experiment)	15.35	39.09	86.80	153.32	244.72
	Freq. (updated model)	15.37	38.75	86.91	153.18	236.03
	MAC	0.999	0.994	0.994	0.992	0.974
S4	Freq. (experiment)	15.17	38.91	84.82	143.24	232.25
	Freq. (updated model)	15.10	39.24	83.80	145.99	233.30
	MAC	1.000	0.998	0.982	0.977	0.898
S5	Freq. (experiment)	15.00	38.98	84.12	143.20	227.94
	Freq. (updated model)	14.91	40.29	83.13	144.46	229.84
	MAC	1.000	0.993	0.981	0.986	0.916
S6	Freq. (experiment)	14.08	33.04	79.93	142.84	219.71
	Freq. (updated model)	13.94	34.60	80.05	144.19	224.47
	MAC	0.999	0.996	0.991	0.967	0.935

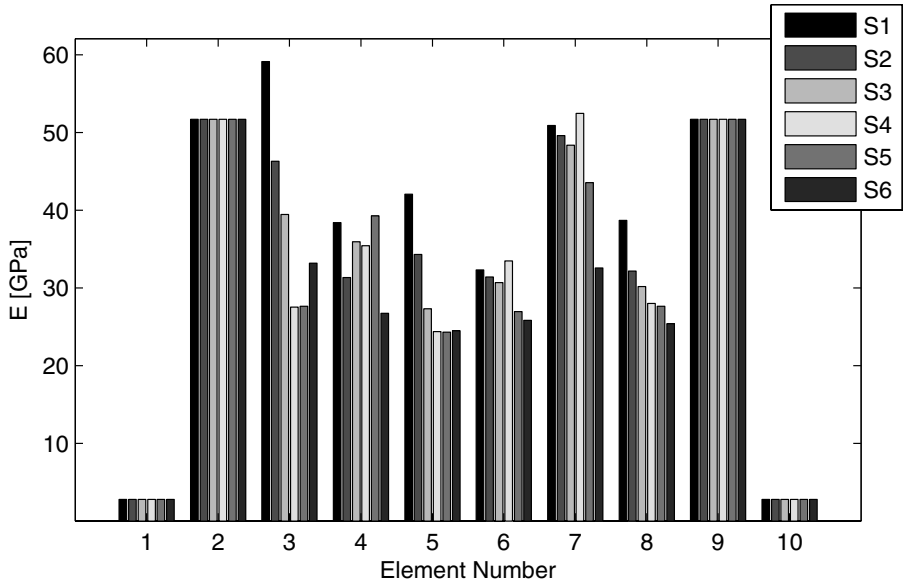

Fig. 20. Updated effective moduli of elasticity of 10 beam elements at different damage states (S1–S6) for first case of damage identification.

Table 10
Effective moduli of elasticity E^e(GPa)/damage factors a^e(%) (relative to reference state S1) of updated elements (# 3–8, 11, 12) at states S2, S3, and S5 for the second case of damage identification

	El. 3	*El. 4*	*El. 5*	*El. 6*	*El. 7*	*El. 8*	*El. 11*	*El. 12*
S2	39.06/34.0	38.23/0.5	38.01/9.6	32.09/0.7	42.85/15.8	36.78/4.9	57.18/0	58.61/55.9
S3	44.07/24.4	38.41/0	27.43/34.8	28.16/12.8	31.37/38.4	35.70/7.7	57.18/0	64.60/51.4
S5	32.28/45.4	38.36/0.1	20.97/50.1	32.01/0.9	29.96/41.2	37.67/2.6	57.18/0	66.16/50.2

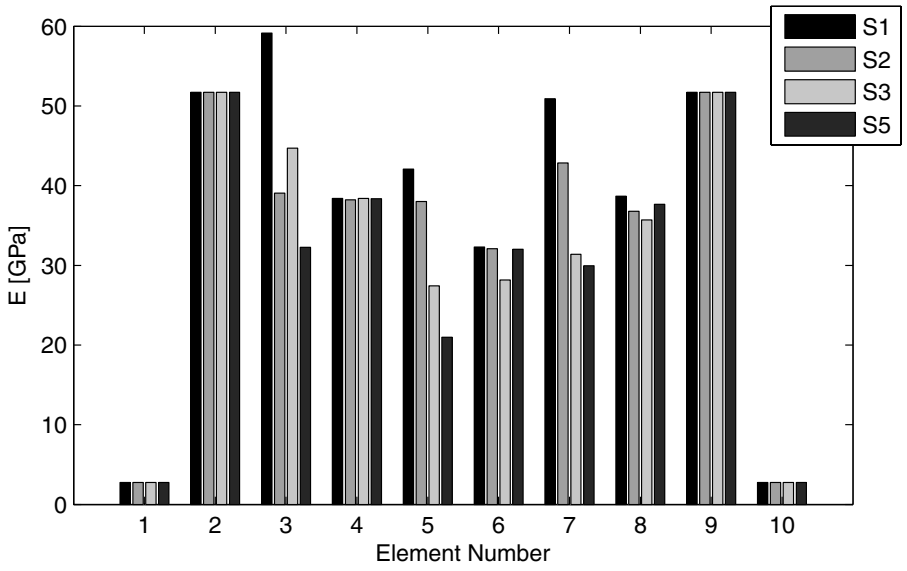

Fig. 21. Updated effective moduli of elasticity of 10 beam elements at different damage states (S1, S2, S3, and S5) for second case of damage identification.

Table 11
Comparison of experimental and analytical modal frequencies (Hz) and MAC values between experimental and analytical mode shapes at states S2, S3, and S5 (second case of damage identification)

		Mode 1	*Mode 2*	*Mode 3*	*Mode 4*	*Mode 5*
S2	Freq. (experiment)	16.09	40.72	89.24	158.90	254.51
	Freq. (updated model)	16.01	38.59	89.19	160.40	–
	MAC (acc. mode shapes)	1.000	0.999	0.988	0.988	–
	MAC (strain mode shapes)	0.997	0.765	0.998	0.987	–
S3	Freq. (experiment)	15.35	39.09	86.80	153.32	244.72
	Freq. (updated model)	15.26	39.20	87.70	156.56	234.31
	MAC (acc. mode shapes)	0.999	0.993	0.995	0.994	0.980
	MAC (strain mode shapes)	0.982	–	0.974	–	–
S5	Freq. (experiment)	15.00	38.98	84.12	143.20	227.94
	Freq. (updated model)	14.71	39.20	84.74	150.14	230.17
	MAC (acc. mode shapes)	1.000	0.995	0.980	0.983	0.933
	MAC (strain mode shapes)	0.972	0.823	0.996	0.937	–

presents the experimentally identified modal frequencies together with their analytical counterparts obtained from the updated FE model as well as the MAC values between experimental and analytical mode shapes (for both displacement and macro-strain mode shapes considered separately) at states S2, S3, and S5. Figure 22 compares the damage factors of all updating elements (3–8, 11, 12) obtained from the two considered cases of damage identification at states S2, S3, and S5. From this figure, it is observed that the damage factors computed from these two cases are in relatively good agreement for elements 3, 5, 6, 11, and 12. Damage is identified along element 4 in the first case and not in the second case. Because FBG sensor # 1 is covering part of element 4 (see Figure 5), it is expected that the results from the second case of damage identification for element 4 are more accurate than those from the first case. In the first case, damage is identified along element 8 with almost no damage along element 7, whereas in the second case, damage is identified along element 7 with very small damage along element 8. Again, the results from the second case of damage identification are expected to be more accurate for elements 7 and 8, because most of FBG sensor #3 is contained in element 8 (see Figure 5). This will be confirmed below by the observed damage in the beam at the end of the experiments. The

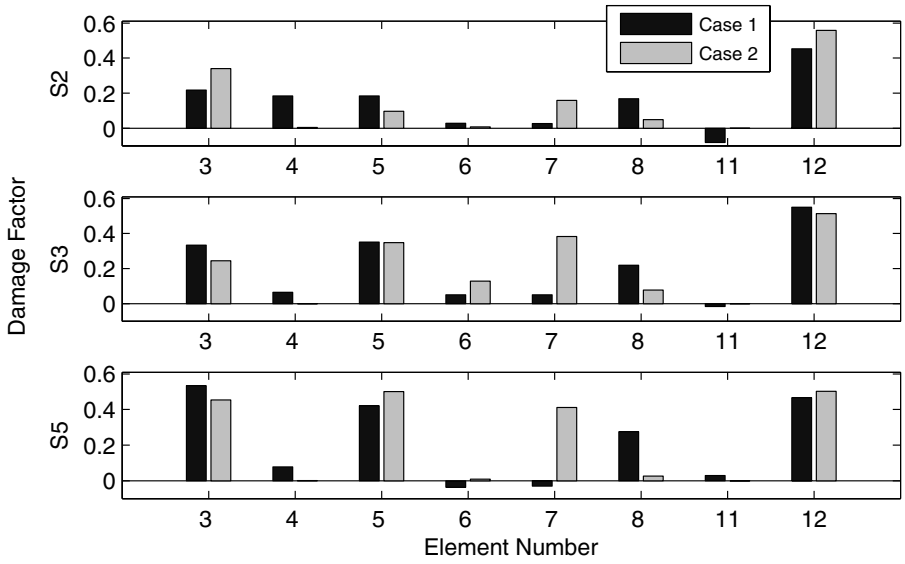

Fig. 22. Comparison of damage factors obtained from the two cases of damage identification at states S2, S3, and S5.

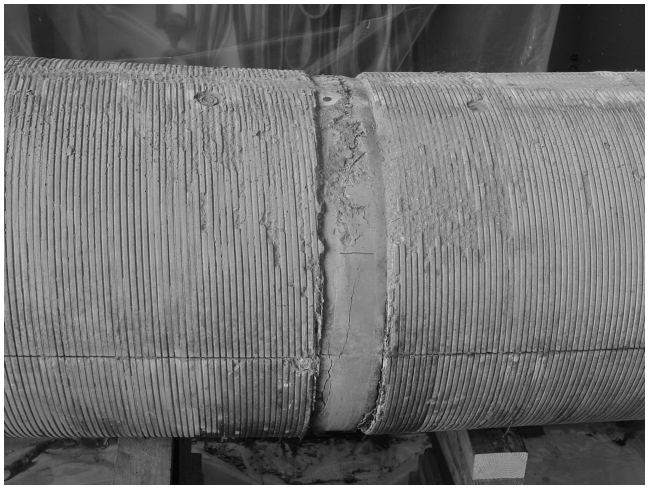

Fig. 23. Damage in the concrete core at the splice location.

differences in the identified damage obtained from the two different cases can be due to: (1) different types of residuals were used in two cases (the addition of macro-strain mode shapes in the second case), and (2) different weights were assigned to residuals in the two cases.

At the end of the experiments, the carbon shell was cut and removed from the concrete core to assess the quality of the infilled concrete and the extent of damage in the concrete, especially in the splice region. Figure 23 shows a picture of the damaged concrete core at the splice location (i.e., mid-span of the girder). Significant flexural cracks can be observed at the top and bottom of the gap region. This gap is located inside element 5 of the FE model (see Figures 5 and 19), and therefore the high damage factors identified at element 5 in both damage identification cases (see Figure 22) are in good agreement with the observed damage. Figure 24 shows local failures in the composite shell at the location of

Fig. 25. Concrete core at northern side of the splice (see Figures 2 and 4).

stirrups both near accelerometer a3 (next to the electrodynamic shaker) inside element 3 (close to element 4) and near accelerometer a7 at the limit between elements 7 and 8. Thus, the damage identification results at elements 3, 7, and 8 (see Figure 22) are consistent with the observed damage in the composite shell. Furthermore, pitted and shrinkage-cracked concrete can be observed in the picture of Figure 25, corresponding to locations of elements 7 and 8, further validating the damage identification results. Finally, it is worth noting that the

(a) (b)

Fig. 24. Composite shell failure at location of stirrup holes: (a) near accelerometer a3, and (b) near accelerometer a7.

large damage factor identified in element 12 (representing the north support) is likely due to the initial friction in the support pin, that is, the pin was not well lubricated initially and broke free during the first set of quasi-static tests leading to state S2.

6 CONCLUSIONS

This article presents the application of a state-of-the-art two-stage damage identification method to a full-scale composite beam (sub-component) based on its measured vibration response. In the first stage, modal parameters (modal frequencies, damping ratios, displacement and macro-strain mode shapes) of the test structure are identified based on its impulse response data measured using accelerometers and long-gage fiber Bragg grating (FBG) strain sensors. In the second stage, changes (from damage state to damage state) in the modal parameters identified in the first stage are used to identify (detect, localize, and quantify) damage in the girder using an element-by-element sensitivity based finite element model updating algorithm. This damage identification study leveraged a full-scale sub-component experiment conducted in the Charles Lee Powell Structural Research Laboratories at the University of California, San Diego, and consisted of uni-directional quasi-static cyclic load tests. After each of several sequences of loading-unloading cycles, a high-quality set of low-amplitude vibration response data was acquired from the beam at various damage levels. Based on impulse (free vibration) response data measured using accelerometers and FBG strain sensors from different impact tests, the Eigensystem Realization Algorithm followed by a least-squares optimization was employed for modal parameter identification of the composite beam in its undamaged (baseline) and various damaged states. The modal identification results from different tests at a given damage state using different types of data (acceleration or macro-strain) show very good agreement, thus validating the system identification results used in the first stage of the damage identification procedure.

The identified modal parameters are then used to identify the damage in the structure using a finite element model updating strategy. Two separate cases of damage identification were performed: (1) the residuals in the objective function used in the FE model updating procedure are based on the natural frequencies and displacement mode shapes identified from accelerometer data, and (2) the residuals are based on the natural frequencies, displacement mode shapes identified from accelerometer data, and macro-strain mode shapes identified from FBG strain sensor data. From the obtained damage identification results, it is observed that the effective moduli of elasticity (used as updating parameters) display an overall decreasing trend with increasing level of damage, which is consistent with the damage-induced stiffness degradation. The updated effective moduli of elasticity obtained from the two different damage identification cases are found to be in relatively good agreement and consistent with the damage observed in the composite beam during and at the end of the experiments. This provides an important validation example for vibration based damage identification using finite element model updating, performed on a full-scale structural component tested in laboratory conditions. However, similar studies are still needed to further evaluate the feasibility of vibration based structural health monitoring for large and complex structures in field conditions.

ACKNOWLEDGMENTS

This work was partially funded by the National Science Foundation, Grant No. DMI-0131967 under a Blue Road Research STTR Project in which UCSD was the principal sub-contractor, and a grant from Lawrence Livermore National Laboratory with Dr. David McCallen as Program Leader. These sources of support are gratefully acknowledged. The authors wish to thank Professor Vistasp Karbhari at UCSD, and Dr. Charles Sikorsky at Caltrans for allowing them to perform the dynamic tests used in this research, as a payload project to their full-scale sub-component experiment. The authors are also grateful to Dr. Michael Fraser for his significant help in acquiring the acceleration data.

REFERENCES

Adeli, H. & Jiang, X. (2006), Dynamic fuzzy wavelet neural network model for structural system identification, *Journal of Structural Engineering, ASCE*, **132**(1), 102–11.

Bernal, D. & Gunes, B. (2004), Flexibility based approach for damage characterization: Benchmark application, *Journal of Engineering Mechanics, ASCE*, **130**(1), 61–70.

Brestel, D., Van Den Einde, Y., Karbhari, V. M. & Seible, F. (2003), Characterization of concrete filled structural formwork, in *Proceedings of the 48th International SAMPE Symposium*, May 11–15, Long Beach, CA, Book 2, 2115–28.

Coleman, T. F. & Li, Y. (1996), An interior Trust Region approach for nonlinear minimization subject to bounds, *SIAM Journal on Optimization*, **6**(2), 418–45.

Conte, J. P. & Liu, M. (2001), Use of long-gage fiber optic sensors for earthquake response monitoring and nondestructive evaluation of structures, *CUREE Report*, Publication No. CKIII-04, CUREE-Kajima Joint Research Program – Phase III.

De Callafon, R. A., Moaveni, B., Conte, J. P., He, X. & Udd, E. (2008), General Realization Algorithm for modal identification of linear dynamic systems, *Journal of Engineering Mechanics, ASCE*, under review.

Doebling, S. W., Farrar, C. R., Prime, M. B. & Shevitz, D. W. (1996), Damage identification in structures and mechanical systems based on changes in their vibration characteristics: A detailed literature survey, *Los Alamos National Laboratory Rep. No. LA-13070-MS*, Los Alamos, NM.

Doebling, S. W., Farrar, C. R. & Prime, M. B. (1998), A summary review of vibration-based damage identification methods, *The Shock and Vibration Digest*, **30**(2), 99–105.

Filippou, F. C. & Constantinides, M. (2004), FEDEASLab getting started guide and simulation examples, *Technical Report NEESgrid-2004–22*, http://fedeaslab.berkeley.edu.

Fox, R. L. & Kapoor, M. P. (1968), Rates of change of eigenvalues and eigenvectors, *AIAAJ*, **6**(12), 2426–29.

Friswell, M. I. & Mottershead, J. E. (1995), *Finite Element Model Updating in Structural Dynamics*, Kluwer Academic Publishers, Boston, USA.

Jiang, X. & Adeli, H. (2005), Dynamic wavelet neural network for nonlinear identification of highrise buildings, *Computer-Aided Civil and Infrastructure Engineering*, **20**(5), 316–30.

Jiang, X. & Adeli, H. (2007), Pseudospectra, MUSIC, and dynamic wavelet neural network for damage detection of highrise buildings, *International Journal for Numerical Methods in Engineering*, **71**(5), 606–629.

Juang, J. N. & Pappa, R. S. (1985), An eigensystem realization algorithm for model parameter identification and model reduction, *Journal of Guidance, Control, and Dynamics*, **8**(5), 620–27.

Maeck, J. & De Roeck, G. (1999), Dynamic bending and torsion stiffness derivation from modal curvatures and torsion rates, *Journal of Sound and Vibration*, **225**(1), 153–70.

MathWorks Inc. (2005), *Matlab – High Performance Numeric Computation and Visualization Software, User's Guide*, The MathWorks Inc., Natick, MA.

Moaveni, B., He, X., Conte, J. P. & Udd, E. (2006), Effect of damage on modal parameters using full-scale test data, in *Proceedings of the International Conference on Modal Analysis (IMAC-XXIV)*, St. Louis, USA.

Pandey, A. K., Biswas, M. & Samman, M. M. (1991), Damage detection from changes in curvature mode shapes, *Journal of Sound and Vibration*, **145**(2), 321–32.

Peeters, B. & De Roeck, G. (2001), Stochastic system identification for operational modal analysis: A review, *Journal of Dynamic Systems, Measurement, and Control*, **123**(4), 659–67.

Salawu, O. S. (1997), Detection of structural damage through changes in frequency: A review, *Engineering Structures*, **19**(9), 718–23.

Seible, F., Hegemier, G. A., Karbhari, V. M., Davol, A., Burgueño, R., Wernli, M. & Zhao, L. (1996), The I-5/Gilman advanced composite cable stayed bridge study, *University of California, San Diego*, SSRP-96/05.

Shi, Z. Y., Law, S. S. & Zhang, L. M. (2002), Improved damage quantification from elemental modal strain energy change, *Journal of Engineering Mechanics, ASCE*, **128**(5), 521–29.

Sohn, H., Farrar, C. R., Hemez, F. M., Shunk, D. D., Stinemates, D. W. & Nadler, B. R. (2003), A review of structural health monitoring literature: 1996–2001, *Los Alamos National Laboratory Report* LA-13976-MS.

Teughels, A. & De Roeck, G. (2004), Structural damage identification of the highway bridge Z24 by finite element model updating, *Journal of Sound and Vibration*, **278**(3), 589–610.